7

Pose Sensor for STIFF-FLOP Manipulator

Sina Sareh[1], Yohan Noh[2], Tommaso Ranzani[3], Min Li[4] and Kaspar Althoefer[5]

[1]Design Robotics, School of Design, Royal College of Art, London, United Kingdom
[2]Centre for Robotics Research, Department of Informatics, King's College London, London, United Kingdom
[3] Department of Mechanical Engineering, Boston University, Boston, MA, United States
[4]Institute of Intelligent Measurement and Instrument, School of Mechanical Engineering, Xi'an Jiaotong University, Xian Shi, China
[5]Advanced Robotics at Queen Mary (ARQ), Faculty of Science and Engineering, Queen Mary University, London, United Kingdom

Abstract

The STIFF-FLOP robotic arm is a cylindrical structure made from soft silicone rubber materials encasing pneumatic actuation chambers. Its material properties and structure allows for the shape, and therefore the pose of the arm, to be dictated by the actuation system as well as by the surfaces with which it is interacting. Although this softness and flexibility makes it inherently safe for many medical and industrial applications, such as keyhole surgery, it comes at the expense of complicating sensing and position control. This chapter presents the main challenges for the development of a pose sensor for soft robotic arms and the STIFF-FLOP approach to tackle them.

7.1 Introduction

Construction of robots using soft materials and components [1–9] promises great potential particularly from the point of view of safe human–robot interaction [10, 11]. However, it is faced with intriguing engineering challenges with respect to configuration and position control [1, 12].

Conventional methods for calculating kinematics and dynamics of robots assume that they are made out of rigid material, their body may only bend where there are joints [13–18], and in the case of a collision with other hard structures and robots, the methods of rigid-body physics are applied [19]. However, the methods are not directly applicable to robots composed from soft and deformable materials, implying the need for bridging the gap by the development of the respective theoretical and experimental methods enabling precise sensing and control in soft robots.

Technologies for hyper-redundant [13–17] and soft [2–8, 20–25] robotic manipulation constitute an important category in soft robotics research with various industrial and medical applications, such as articulated robotic tools for operation in confined spaces, e.g., STIFF-FLOP [3, 19–25]. The tools are usually made from mutually-tangent curved segments enabling high degrees of robotic articulation in hard-to-access, unstructured, and cluttered workspaces [3, 26]. However, control of these robots requires precise sensing of the robot's pose—information on the position and orientation of the robot end-effector—and shape—information on the robot's articulated body form.

The complex shape generated by these robots have been mainly tracked through incorporation of vision systems [27] and electromagnetic tracking [28]; these visual techniques are often restricted with visual occlusion and electromagnetic tracking; they are subject to magnetic field distortions and have limitations with regard to the mobility of the magnetic field generation system. However, the required information on the complex shape and pose of the robot can be obtained through an appropriate multi-segment flex sensing method [29].

A number of sensing mechanisms for measuring the flexion have been proposed in the literature. Prominent examples include: off-the-shelf resistive flex sensors based on conductive ink, e.g., *FLXT* (Flexpoint Sensor Systems, Inc., United States); flexible sensors based on specific types of smart materials, e.g., *Ionic Polymer Metal Composite (IPMC)* [30]; soft sensors based on the micro-channel of conductive liquid (Eutectic Gallium Indium, *eGaIn*) [31]; and sensing systems based on fiber optics. Resistive sensors based on conductive inks and IPMCs are bipolar devices and are not usually suitable for three-dimensional fabrication. The sensing systems based on eGaIn are attractive for integration in soft structures and robots; however, there is no data on biocompatibility of this material according to the datasheet published. Sensors based on fiber optics function by measuring the change in optical characteristics of the light [4, 19, 26, 32–37]. From the electrical point of view, optical fibers are immune to magnetic fields and electrical interference and hence, they are distinguished candidates for many industrial and medical

applications. From the mechanical point of view, plastic optical fibers are very attractive for integration into soft structures due to their ability to follow the elastic deformation of the robot bodies in which they are embedded. Optical sensors based on Fiber Bragg Grating are costly and sensitive to temperature and strain [34, 38].

STIFF-FLOP employed light intensity modulation to produce a low-cost multi-segment optical curvature sensor amenable to being integrated into for flexible, soft and extensible robotic arms [26, 29, 32]. In the following, the design challenges and STIFF-FLOP approaches in implementation and testing of the pose-sensing system are discussed; starting with sensing solutions for a one-segment STIFF-FLOP arm (also referred to as STIFF-FLOP module) as well as generalization of the method for use in a multi-segment manipulator.

7.2 Design of the Pose-sensing System

7.2.1 Pose-sensing in a One Segment STIFF-FLOP Arm

The pose sensor of each segment of the arm consists of three optical fibers sliding inside flexible housings in the periphery of the arm, as illustrated in Figures 7.1a and b, in parallel with actuation chambers. When the arm bends, the optical fibers' length portion inside the flexible arm (s_1, s_2, and s_3) will change according to the pose (amount of flexure and the tip orientation) of the arm; it causes a change in the position of the light-emitting optical fibers and, consequently, the intensity of the light received by light detectors, e.g., FS-N11MN (Keyence$^{\mathrm{TM}}$, Japan). The received light is then converted into voltage $v = [v_1\ v_2\ v_3]$ and related to the corresponding distance vector $s = f\ (v) = [s_1\ s_2\ s_3]$, to acquire configuration parameters of the arm segment for each specific pose. The configuration parameters are as follows: S is the length of the central axis of each segment, θ is the bending angle, and φ is the orientation angle, and can be expressed as,

$$S = \frac{1}{3}\sum\nolimits_{i=1}^{3}(S_i) \tag{7.1}$$

$$\theta = \frac{S - s_1}{d.\cos(\frac{\pi}{2} - \varphi)} \tag{7.2}$$

$$\varphi = \tan^{-1}\left(\frac{\sqrt{3}\,(s_2 + s_3 - 2s_1)}{3\,(s_2 - s_3)}\right) \tag{7.3}$$

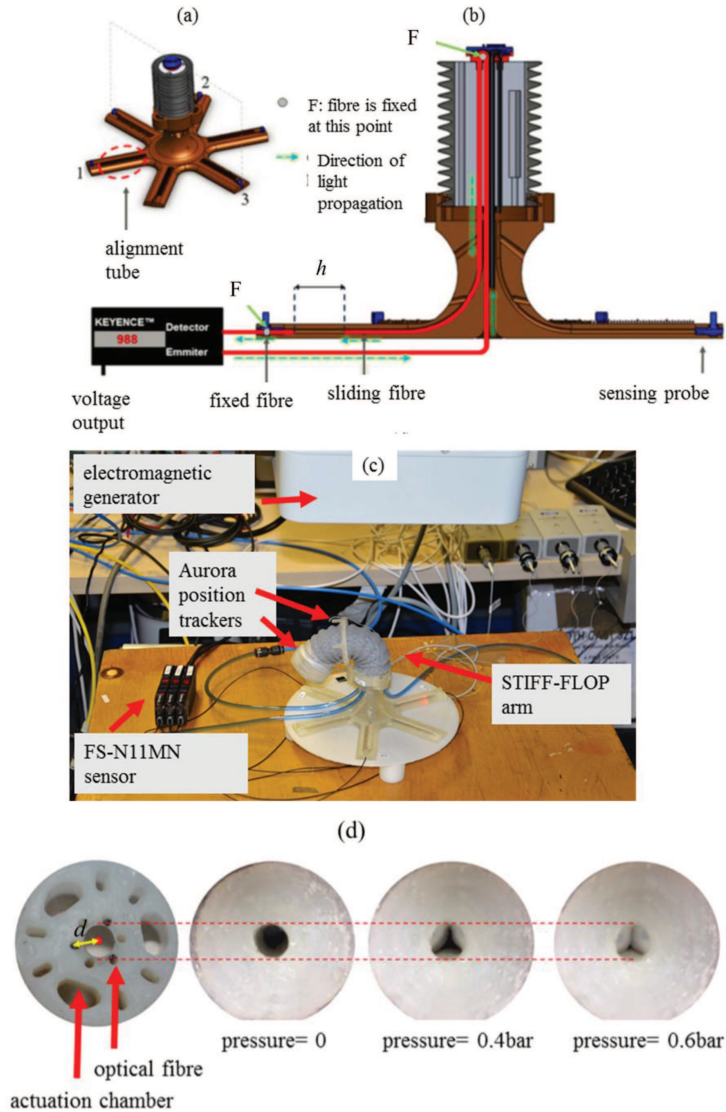

Figure 7.1 (a) The overall structure of the STIFF-FLOP module with integrated bending sensor, (b) the experimental configuration for measuring the flexure angle; four Aurora electromagnetic trackers are integrated at the base, tip and on the body of the arm, (c) the cross section of the module indicating the position of pneumatic actuators and optical fiber, and (d) the top view of the module indicating the negative impact of actuation chambers on the sensing system; increasing the pressure inside the actuation chambers results in a ballooning effect toward the internal hollow structure which changes the radial location of optical fibers used for pose-sensing.

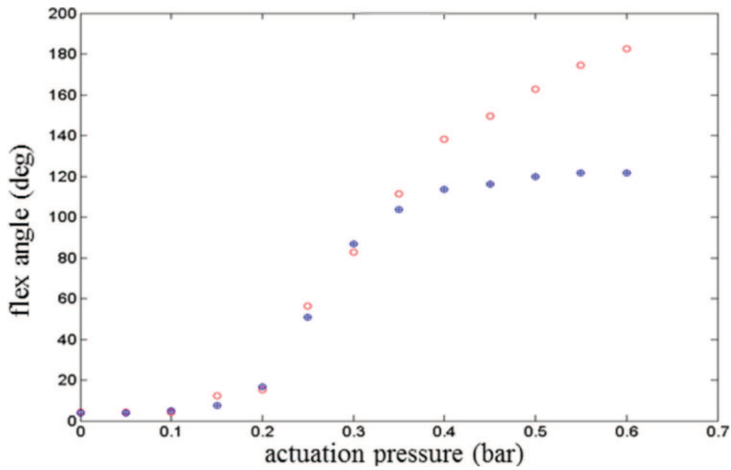

Figure 7.2 The experimental curvature sensing results for the experimental configuration described in Figure 7.1.

Variable d in Equation (7.2) describes the distance between the central axis of the arm segment and the parallel optical fibers. Being integrated into a soft structure, this distance between components of the sensing system may change during the operation of the arm by the internal actuation system or via externally applied forces and directly affect its resolution. The experimental setup for measuring the flexure angle is shown in Figure 7.1c where an Aurora electromagnetic tracking system is used for benchmarking. The experimental results (Figure 7.2) show an error of more than 20° when pressuring a single channel up to 0.4 bar with an increasing trend for larger amounts of input air pressure which is due to the movement of optical fibers by the parallel actuation chambers, as shown in Figure 7.1d.

To overcome the aforementioned problem, the STIFF-FLOP pose-sensing system considered the following: (1) in order to increase the robustness of the sensors, no optical fibers should be sent inside the soft arm and (2) an internal support structure that can maintain the radial location of the sensing components inside the soft structure of the arm should be added to protect the sensing system against the unwanted relative motion dictated by the actuation system.

Hence, a flexible internal structure responsible for maintaining the radial distance between passive cables and the center of the flexible arm during manipulations at the distal side was created along with a distance modulation array which couples the motion of passive cables with light-emitting optical

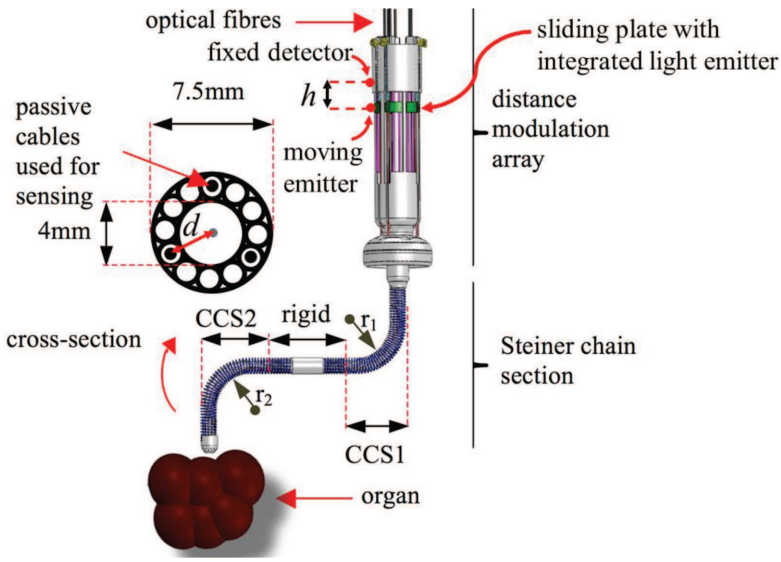

Figure 7.3 The two-segment arm with an integrated pose-sensing system in a surgical scenario interacting with an organ. The flexible Steiner chain section also provides an empty central channel for end-effector tools (CCS1 and CCS2 indicate constant curvature segments with radii of r_1 and r_2, respectively).

fibers using a low-friction sliding mechanism at the proximal side. The light-emitting optical fiber is paired and aligned with optical detectors fixed at the base of the arm, as illustrated in Figure 7.3.

The pose-sensing principle employs multiple passive cables passed through 1.2 mm (outer diameter) spring channels integrated along the length of the arm (50 mm in length). These channels are located at the same distance d from the central axis of the arm but using different equally spaced angular positions. The cable channels are continued outside the arm using the 3D printed part of the sensor where they are converted to sliding rails. A very low-friction sliding mechanism was created employing two steel needles with thickness of 0.89 mm located parallel to and 4 mm away from each other. A specialized U-shaped mechano-optical coupler[1] was designed and fabricated to be able to smoothly slide around needles and carry the light-transmitting optical fibers inside the sensor base. The sliding plate is linked with a 2 mm outer diameter extension spring which is fixed at one side and

[1]The interface between passive cables of the Steiner chain section and optical fibers of the distance modulation array.

enables retraction and position recovery after being pulled by cables. This arrangement allows the pose sensor to exploit a retractable sliding mechanism for modulating the distance between emitter and detector optical fibers.

7.2.2 The Flexible Steiner Chain Section

In geometry, a Steiner chain is a set of mutually tangent n circles, all of which are tangent to two given non-intersecting circles, as illustrated in Figure 7.4a. The Steiner chain mathematics can explain the design of a steerable endoscope in [39], using low-cost commercial springs; the springs are tangentially combined in parallel to tightly accommodate driving tendons and prevent their radial displacement. Figure 7.4a also describes the cross-section of the endoscopic mechanism; note that the structure can also house passive cables to code the shape of the endoscope or similar manipulation systems. In the following, we will report on the Steiner chain implementation of STIFF-FLOP's pose-sensing system and the details of the new design.

Referring to Figure 7.4b and Equations (7.1) to (7.3), the amount of change in values of s_1, s_2, and s_3 due to a bending is in a direct relationship with d. Therefore, d is directly affecting the resolution of the sensor system: By substituting $\varphi_1 = \frac{\pi}{2}$ and a very small amount of bending $\theta_1 = \frac{\pi}{180}$ in Equations (7.3) and then (7.2)

$$-2s_{1,1} + s_{2,1} + s_{3,1} = 0.0525d \tag{7.4}$$

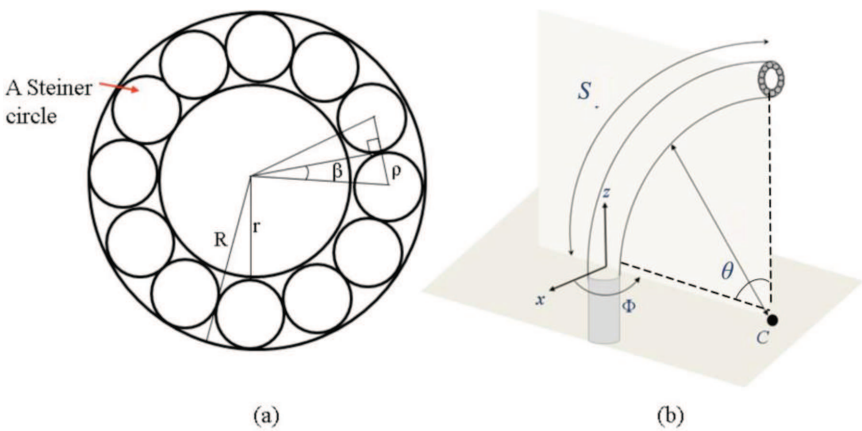

Figure 7.4 (a) The Steiner chain cross-section of the arm and (b) the flexed configuration of the arm and associated parameters in 3D [38].

where $s_{i,1}$ denotes the primary length of the cable *i* which is inside the arm segment. Also from Equation (7.3), $s_{2,1} = s_{3,1}$, therefore, it yields

$$s_{2,1} - s_{1,1} = 0.0262d \tag{7.5}$$

If substituting $\varphi_2 = \frac{\pi}{2}$ and $\theta_2 = \frac{\pi}{2}$ in the same set of equations

$$s_{2,2} - s_{1,2} = \frac{3\pi}{4}d, \tag{7.6}$$

where $s_{i,2}$ explains the secondary length of the cable *i* which is inside the arm segment. Therefore the total change in the length of the cable s_1 can be obtained by subtracting Equations (7.5) and (7.6)

$$\Delta s_1 = s_{2,2} - s_{1,2} - s_{2,1} + s_{1,1} \tag{7.7}$$

The arm segments are made from extension springs and therefore are incompressible. Assuming $s_{2,2} \approx s_{2,1}$, the change in the cable's length inside the arm can be calculated through

$$\Delta s_1 \approx \frac{3\pi}{4}d \tag{7.8}$$

The KEYENCE FS-N11MN fiber optic light-to-voltage convertor used in this study can effectively measure a maximum fiber length change of 20 mm. In order to measure a 90° bending deformation, the maximum value of *d* ($d_{\max}$) must not exceed 8.4 mm. It is clear that, this value should be reduced to 4.2 mm for measuring a maximum of 180° bending which can be regarded as two successive 90° bending as targeted in this study. Since the maximum combined deformation of the two segments should be also measureable within the 20 mm range, the maximum value of the *d* parameter, $d_{\max}$, needs to be 2.1 mm.

In order to preserve the maximum resolution of the sensing system, we choose the maximum value for *d*, which is 2.1 mm. This needs incorporating of an inner spring with a diameter of slightly less than 4 mm. Therefore a LEM050AB 05 S stainless steel extension spring (Lee Spring Ltd., United States) with an outer diameter of 3.505 mm, a wire diameter of 0.508, and a stiffness rate of 0.04 N/mm was used as the central spine. To implement Steiner springs which correspond to Steiner circles in the cross-section view, see Figure 7.4a, custom springs with an outer diameter of 1.2 mm and a wire diameter of 0.25 mm were used. Steel passive cables with a diameter of 0.27 mm (Carl Stahl Ltd., Germany) were radially fixed at approximately

d = 2.1mm away from the center. The central angle $\beta = \sin^{-1}\left(\frac{\rho}{r+\rho}\right)$ is approximately 15°, the number of Steiner springs is $n = \frac{180}{\beta} = 12$, and the inner diameter of the outer spring is approximately $R = r + 2\rho = 5.91$ mm. Therefore, LEM070CB 05 S (Lee Spring Ltd., United States) with an outer diameter of 7.49 mm and a wire diameter of 0.711 mm was selected.

7.2.3 Design of a Low-friction Retractable Distance Modulation Array

When the arm bends, the portion of length of each passive cable which is inside the arm will change. As it returns to its original straight configuration, the cables' length portion inside the arm are also required to return to their original state. Several reasons including friction, and hysteresis in the mechanical structure and material properties prevent meeting this essential condition and introduce malfunction into the pose-sensing system. In order to make sure the mutual distance between the emitting and detecting fiber optic pairs is recovered, a spring returning mechanism is a straightforward solution. In addition, this mechanism couples the motion of passive cables that are passed through the length of the flexible arm with optical fibers for light intensity measurement using KEYENCE convertors.

7.2.3.1 Loopback design of the optical system

The *commercial off-the-shelf* stretch (length) sensors are usually fabricated to be free from electronics at one end. Examples of such implementation include stretch sensors from StretchSense Ltd, New Zealand, and PolyPower® Stretch Sensors. This free end is usually coupled with the moving end of the actuator to measure the length change. In our work, in order to allow all the electronics to be at one end of the sensor, we used a U-shape arrangement of optical fibers to produce a loopback configuration. This enables placing the emitter and detector next to each other, as illustrated in Figure 7.5b.

7.2.3.2 Steel spring-needle double slider

Modulating the mutual distance between any pair of optical fibers required a low-friction sliding mechanism to be designed and implemented. We manufactured a highly smooth double slider, which uses two steel needles (44 mm length × 0.86 mm diameter, John James Needles, Worcestershire, England). The needles were surrounded by two pieces of miniature steel springs (1.4 mm outer diameter, 0.2 mm wire diameter) installed in parallel

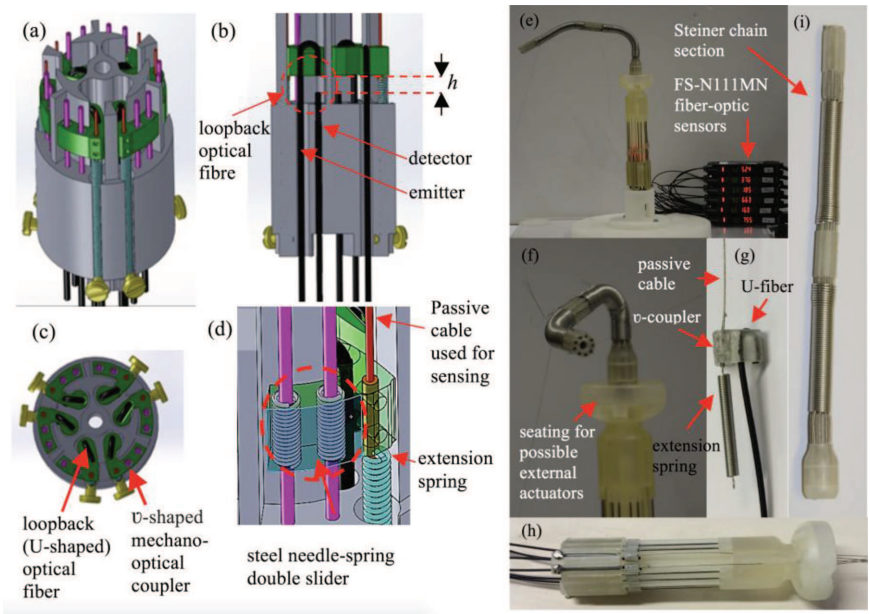

Figure 7.5 The CAD designs of the multi-segment flex sensor exhibiting integrated technologies: (a) the side view showing the elastic recovery mechanism of the slider, (b) the low-friction steel spring-double needle sliding mechanism to maintain the direction of the motion, (c) the U-shaped fiber optic arrangement, (d) close-up view of the sliding mechanism. The prototype of the arm and sensing system: (e) the finished configuration of the sensorized manipulation system, (f) close-up view of the top part, (g) the U-shaped mechano-optical coupler, (h) the fully assembled structure of the distance modulation array, and (i) the structure of the Steiner chain section.

and 4 mm away from each other into the plastic sensor base. Each steel spring that was able to smoothly slide around the surrounded needle, was embedded into a U-shaped plastic mechano-optical coupler. Each coupler linked a passive cable with its associated fiber optic pair. This mechanism is shown in Figure 7.5d. Note that Figure 7.5c shows the cross-section of the distance modulation array, highlighting its internal structure.

7.3 Fabrication and Assembly of the Pose-sensing System

The sensorized arm in its finished configuration is shown in Figures 7.5e and f. The structure of the mechano-optical coupler is shown in Figure 7.5g. It comprises a U-shaped 3D printed part with a U-shaped housing for an

optical fiber, and a connection module which connects a 2 mm outer diameter extension spring (Lee Spring Ltd., United States), with a 0.27 mm thick steel wire rope (Carl Stahl, Germany), used as the passive cable. The 2 mm extension springs are in charge of cables position recovery and therefore are referred to as recovery springs. In order to increase the pulling force, an initial stretch of 5 mm for the recovery springs was considered. Finally, Figures 7.5h and i describe the full assembled structure of the main Steiner chain, and distance modulation array parts of the flexible arm. All plastic parts were manufactured using 3D printing (Projet HD-3000 Plus 3D Systems).

7.4 Sensor Calibration and Benchmarking

A set of experiments were performed to validate the design and implementation of the two-segment pose sensor in which either one or both of the segments were actuated at a time. Two high-definition (HD) cameras were placed at the top and side of the arm to record ground truth flex information. The middle and tip of the arm were attached to fixed points on the wall, using steel wires to generate stable shape patterns, as our experimental prototype was not yet equipped with motors or any other actuation system. Subsequently we have recorded the light intensity (and respective voltage values) from KEYENCE optical convertors and HD cameras.

To convert voltage values to corresponding values of distance between optical fiber tips h, the calibration relationships for all six fiber optic channels were extracted. The averaged calibration data, presented in Figure 7.6, was splined using MATLAB (MathWorks, Inc., Natick, MA, United States) software to form the calibration curve (over five trials).

After the calibration of sensors, the arm was forced into various 3D shapes, as shown in Figure 7.7, and the sensor voltage signals were recorded for analysis. In order to use the constant curvature bending model, the acquired voltage signals were fed into the splined calibration curve of Figure 7.6 to back-calculate the tip-to-tip fiber optic distances. Then, these distances were substituted into Equations (7.2) and (7.3) to calculate the flexion of the arm. Figure 7.8b shows the experimental results compared with their respective ground truth information extracted from HD camera images using a custom MATLAB code.

Figure 7.8a, $s_{i,j}$ represents the tip-to-tip distance between the optical fiber pair, where $i = \{1,2,3\}$ is the pair number and $j = \{1,2,3,4,5\}$ is the trial number. The trend in $\alpha = s_{i,j}/V_{i,j}$ implies that the arm was bent approximately symmetric with respect to cables b_1 and b_3, where these

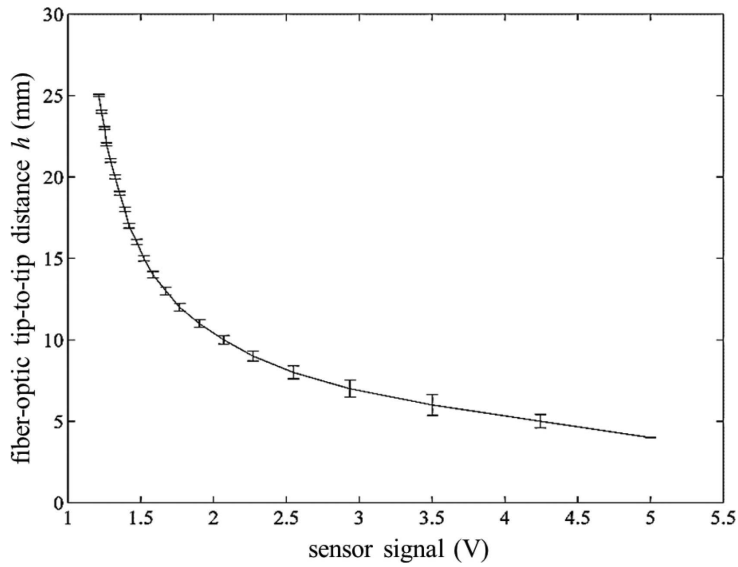

Figure 7.6 The averaged calibration curve and error bars.

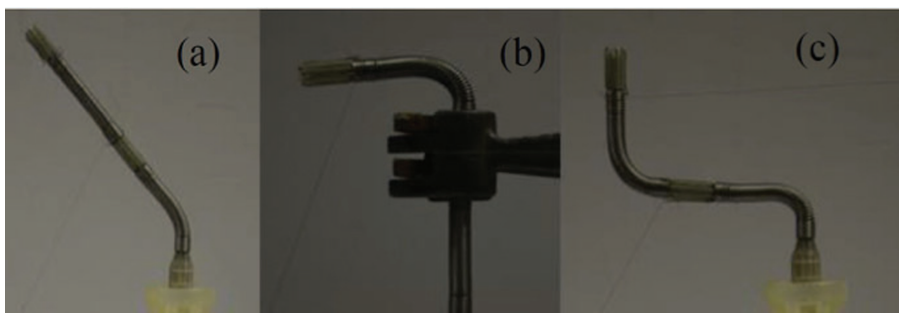

Figure 7.7 Examples of key experimental configurations: (a) independent activation of base segment, (b) independent activation of the tip segment (note that the intersegment link is clamed to produce a stationary base), and (c) simultaneous activation of two segments.

two cables are virtually stretched (note that only the length portion of the cables inside the arm can change physically). The cable b_2 was only slightly compressed, with respect to the length change in the other two cables which confirms the design assumption that led to Equation (7.6).

Figure 7.8b shows the experimental results where segments of the arm were bent individually, which implies a maximum tracking error of around 7° in the tip segment when the arm was bent with ground truth value of 40°.

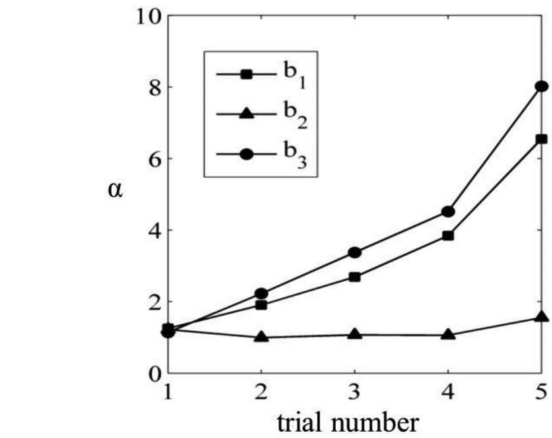

(a)

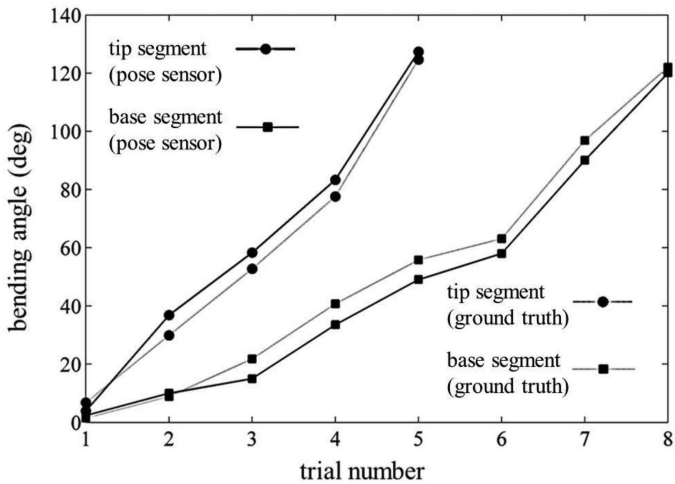

(b)

Figure 7.8 (a) The $\alpha = s_{i,j}/V_{i,j}$ values for the base segment experiment, b_n is a cable number, and (b) the experimental results of flex sensing in individual segments.

This error was decreased to 5° as the arm reached a ground truth flexion of 63° and around 2° for ground truth value of 122°. A similar behavior can be seen in the flex data of the base segment, also presented in Figure 7.7b. The finer function of the sensor for large amounts of flexion can be relevant for better positioning of cables inside the spring channels. The channels have

an internal diameter of around 0.8 mm and house two 0.27 mm-thick cables along the length of the base segment, and only one of them along the length of the tip segment, which gives some room for the cables to play radially, if they are not pulled tightly using extension springs. The experimental results imply that the error can be reduced if this initial stretch is increased from the 5mm (the original amount of initial stretch in our design).

7.5 Calculation of the Bending Curvature in a Two-segment Arm Based on Collocated Cables

To simplify the multi-segment flexion sensing, this work used a method referred to as "collocated cables." This sensing arrangement uses only 3 Steiner channels out of the 12 for sensing. There are two passive cables sliding inside each of these three channels; one fixed between two segments and the other one at the tip of the arm. This arrangement enables measuring the flex angle in multi-segment arms in a modular way and with minimal amendment in the cables' length computation. When the arm undergoes a complex two-segment movement, the change in the length of cables passing through the whole length of the arm to the tip (t-type cables t_1, t_2, and t_3), is only partially because of the flexion of the tip segment. However, the change in the length of the fibers fixed at the tip of the base segment (b-type cables b_1, b_2, and b_3) is purely due to the flexion in this segment. In our sensing arrangement, each t-type cable is accompanied by a b-type cable, as shown in Figure 7.9. This method allows calculating the share of each segment from the total length change.

To intuitively evaluate this method, the segments of the arm were forced into a complex S-shape configuration, as shown in Figure 7.6c. Using camera ground truth information, we have calculated the flexion angle in two segments as $\theta_{\text{Ground},1} = 91.2°$, $\theta_{\text{Ground},2} = 95.1°$.

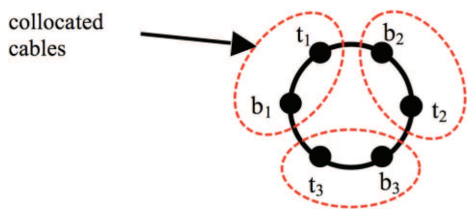

Figure 7.9 The cross-section of the distance modulation array, showing the collocated arrangement of passive cables used for sensing.

Table 7.1 Calculation of the pure length change in each segment based on collocated cables approach

Voltage (V)	V_{b1}	V_{b2}	V_{b3}	V_{t1}	V_{t2}	V_{t3}
	3.99	2.92	1.93	1.89	2.27	1.93
Length (mm)	s_{b1}	s_{b2}	s_{b3}	s_{t1}	s_{t2}	s_{t3}
	5.34	7.04	10.87	11.11	9.01	10.87
Length (mm)	s_{p1}		s_{p2}		s_{p3}	
	5.77		1.96		0	

Table 7.1 summarizes the calculation of length change in each segment based on the collocated cables' lengths; V_{bi} values, i = {1,2,3}, represent FS-N11MN voltage readings associated with cables that are fixed between two segments; V_{ti} are readings associated with cables passed through the whole length of the arm and fixed at the tip. Mapping into the splined voltage-distance relationship (Figure 7.6), the corresponding fibers' mutual distances s_{bi} and s_{ti} were calculated. Whilst values of s_{bi} represent the pure length change in the base segment, the pure length change of the tip segment can be computed through $s_{pi} = s_{ti} - s_{bi}$.

By substituting pure distance values into Equations (7.1) to (7.3), the flexion angles are computed as $\theta_{\text{Sensor},1} = 89.2^\circ$ and $\theta_{\text{Sensor},2} = 92.4^\circ$, implying an error of less than 3° in each segment.

7.6 Conclusion

In this chapter, we have presented the design and implementation of a pose-sensing system for soft robot arms. Starting from theoretical design, the radial location of the passive cables used for sensing along the periphery of the arm were optimized. This optimization work presents a trade-off between maximum compactness of the sensing system and using the full resolution of the optical measurement system. In the next step, we have presented a Steiner chain design for the flexible part of the sensor system. Three (out of twelve) Steiner chain channels were used for pose-sensing in the two-segment flexible arm. Subsequently, a low-friction fiber-optic distance modulation array based on a new spring-needle double slider we designed and implemented to precisely measure the change in the length of cables embedded in the periphery of the arm. The sensing system also features a loopback optical design to keep all electronics away from of the sensing site.

The sensing system is experimentally validated resulting in a maximum error of 6°, with respect to the camera ground truth information in measuring

the flexion angle in individual segments. From the experimental results, it can be implied that the sensor's error can be reduced by increasing the initial stretch length of recovery springs, to make a tighter cabling system in low flexion. We have also demonstrated and discussed multi-segment flex sensing using collocation of passive cables in mutually-tangent (successive) segments. This sensing system can be regarded as complementary to the two-segment soft actuation system presented in [20].

Acknowledgment

The work described in this paper is funded by the Seventh Framework Programme of the European Commission under grant agreement 287728 in the framework of EU project STIFF-FLOP.

References

[1] Rus, D., and Tolley, M. T. (2015). Design, fabrication and control of soft robots. *Nature* 521, 467–475.

[2] Trivedi, D., Rahn, C. D., Kier, W. M., and Walker, I. D. (2008). Soft robotics: biological inspiration, state of the art, and future research. *Appl. Bionics Biomech.* 5, 99–117.

[3] Cianchetti, M., Ranzani, T., Gerboni, G., Nanayakkara, T., Althoefer, K., Dasgupta, P., et al. (2014). Soft robotics technologies to address shortcomings in today's minimally invasive surgery: the STIFF-FLOP approach. *Soft Robot.* 1, 122–131.

[4] Sareh, S., Althoefer, K., Li, M., Noh, Y., Tramacere, F., Sareh, P., et al. (2017). Anchoring like octopus: biologically inspired soft artificial sucker. *J. R. Soc. Interface* 14:20170395.

[5] Kim, S., Laschi, C., and Trimmer, B. (2013). Soft robotics: a bioinspired evolution in robotics. *Trends Biotechnol.* 31, 287–294.

[6] Stilli, A., Wurdemann, H. A., and Althoefer, K. (2014). "Shrinkable stiffness-controllable soft manipulator based on a bio-inspired antagonistic actuation principle," in *Proceedings of the IEEE/RSJ International Conference on Intelligent Robots and Systems*, Madrid.

[7] Sareh, S., Conn, A. T., and Rossiter, J. M. (2010). "Optimization of bio-inspired multi-segment IPMC cilia," in *Proceedings of the Electroactive Polymer Actuators and Devices (EAPAD XII),* Vol. 7642, (Bellingham, WN: SPIE).

[8] Rossiter, J., and Sareh, S. (2014). "Kirigami design and fabrication for biomimetic robotics," in *Proceedings of the SPIE 9055, Bioinspiration, Biomimetics, and Bioreplication, 90550G* (Bellingham, WN: SPIE).

[9] Kim, J., Alspach, A., and Yamane, K. (2015). "3d printed soft skin for safe human-robot interaction," in *Proceedings of the Intelligent Robots and Systems (IROS), 2015 IEEE/RSJ International Conference on IEEE*, Madrid, 2419–2425.

[10] Schiavi, R., Grioli, G., Sen, S., and Bicchi, A. (2008). "Vsa-ii: a novel prototype of variable stiffness actuator for safe and performing robots interacting with humans," in *Proceedings of the IEEE International Conference on Robotics and Automation* (Rome: IEEE), 2171–2176.

[11] Marchese, A. D., Komorowski, K., Onal, C. D., and Rus, D. (2014). "Design and control of a soft and continuously deformable 2D robotic manipulation system," in *Proceedings of IEEE International Conference on Robotics and Automation,* Singapore.

[12] Yamada, H., Chigisaki, S., Mori, M., Takita, K., Ogami, K., and Hirose, S. (2005). "Development of amphibious snake-like robot ACM-R5," in *Proceedings of the 36th International Symposium Robotics*, Tokyo, 133.

[13] Lipkin, K., Brown, I., Peck, A., Choset, H., Rembisz, J., Gianfortoni, P., et al. (2007). "Differentiable and piecewise differentiable gaits for snake robots," in *Proceedings of the IEEE International Conference on Intelligent Robots and Systems*, San Diego, CA, 1864–1869.

[14] Shang, J., Noonan, D., Payne, C., Clark, J., Sodergren, M. H., Darzi, A., et al. (2011). "An articulated universal joint based flexible access robot for minimally invasive surgery," in *Proceedings of the IEEE International Conference on Robotics and Automation*, Brisbane, QLD, 1147–1152.

[15] Degani, A., Choset, H., Zubiate, B., Ota, T., and Zenati, M. (2008). "Highly articulated robotic probe for minimally invasive surgery," in *Proceedings of the 30th Annual International IEEE EMBS Conference*, Vancouver, BC.

[16] OC Robotics (2008). *Snake-arm Robots Access the Inaccessible*. Bristol: OC Robotics, 92–94.

[17] Sareh, P., and Kovac, M. (2017). Mechanized creatures. *Science* 355:1379.

[18] Sklar, E., Sareh, S., Secco, E., Faragasso, A., and Althoefer, K. (2016) A non-linear model for predicting tip position of a pliable robot arm segment using bending sensor data. *Sens. Trans.* 199, 52–61.

[19] Ranzani, T., Gerboni, G., Cianchetti, M., and Menciassi, A. (2015). A bioinspired soft manipulator for minimally invasive surgery. *Bioinspir. Biomim.* 10:035008.

[20] Sareh, S., Rossiter, J. M., Conn, A. T., Drescher, K., and Goldstein, R. E. (2013). Swimming like algae: biomimetic soft artificial cilia. *J. R. Soc. Interface* 10:0666.

[21] Robertson, M. A. and Paik, J. (2017). New soft robots really suck: vacuum-powered systems empower diverse capabilities. *Sci. Robot*. 2:eaan6357.

[22] Noh, Y., Sareh, S., Wrdemann, H., Liu, H., Housden, J., Rhode, K., et al. (2015). A three-axial fiber-optic body force sensor for flexible manipulators. *IEEE Sens. J.* 99, 1641–1651.

[23] Sareh, S., Jiang, A, Faragasso, A., Noh, Y., Nanayakkara, T., Dasgupta, P., et al. (2014). "Bio-inspired tactile sensor sleeve for surgical soft manipulators," in *Proceedings of the IEEE International Conference on Robotics and Automation (ICRA 2014)*, Hong Kong.

[24] Wurdemann, H. A., Sareh, S., Shafti, A., Noh, Y., Faragasso, A., Chathuranga, D. S., et al. (2015). "Embedded electro-conductive yarn for shape sensing of soft robotic manipulators," in *Proceedings of the 37th Annual International Conference of the IEEE Engineering in Medicine and Biology Society (EMBC)*, Milano, 8026–8029.

[25] Sareh, S., Noh, Y., Ranzani, T., Würdemann, H., Liu, H., and Althoefer, K. (2015). "Modular fibre-optic shape sensor for articulated surgical instruments," in *Proceedings of the Hamlyn Symposium on Medical Robotics*, London.

[26] Croom, J. M., Rucker, D. C., Romano, J. M., and Webster, R. J. (2010). "Visual sensing of continuum robot shape using self-organizing maps," in *Proceedings of the IEEE International Conference on Robotics and Automation*, Singapore, 4591–4596.

[27] Mahvash, M., and Dupont, P. E. (2010). "Stiffness control of a continuum manipulator in contact with a soft environment," in *Proceedings of the IEEE/RSJ International Conference on Intelligent Robots and Systems,* Madrid, 863–870.

[28] Sareh, S., Noh, Y., Ranzani, T., Würdemann, H., Liu, H., and Althoefer, K. (2015). "A 7.5 mm Steiner chain fibre-optic system for multi-segment flex sensing," in *Proceedings of the IEEE/RSJ in International Conference on Intelligent Robots and Systems (IROS)*, Vancouver, BC, 2336–2341.

[29] Punning, A., Kruusmaa, M., and Abaloo, A. (2007). Surface resistance experiments with IPMC. *Sens. Act. A* 133, 200–209.

[30] Vogt, D. M., Yong-Lae, P., and Wood, R. J. (2013). Design and characterization of a soft multi-axis force sensor using embedded microfluidic channels. *Sens. J. IEEE* 13, 4056–4064.

[31] Sareh, S., Noh, Y., Li, M., Ranzani, T., Liu, H. and Althoefer, K. (2015). Macrobend optical sensing for pose measurement in soft robot arms. *Smart Mater. Struct.* 24:125024.

[32] Ryu, S., and Dupont, P. E. (2014). "FBG-based shape sensing tubes for continuum robots," in *Proceedings of the IEEE International Conference on Robotics and Automation*, Singapore, 3531–3537.

[33] Zhang, X., Max, J. J., Jiang, X., Yu, L., and Kassi, H. (2007) "Experimental investigation on optical spectral deformation of embedded FBG sensors," in *Proceedings of the SPIE 6478, Photonics Packaging, Integration, and Interconnects VII*, San Jose, CA.

[34] Polygerinos, P., Seneviratne, L. D., and Althoefer, K. (2011). Modeling of light intensity-modulated fibre-optic displacement sensors. *Act. Instr. Meas.* 60, 1408–1415.

[35] Noh, Y., Liu, H., Sareh, S., Chathuranga, D., Wurdemann, H., Rhode, K., et al. (2016). Image-based optical miniaturized three-axis force sensor for cardiac catheterization. *IEEE Sens.* 16, 7924–7932.

[36] Patrick, H., Chang, C., and Vohra, S. (1998). Long period fibre gratings for structural bend sensing. *Electron. Lett.* 34, 1773–1775.

[37] Yi, J., Zhu, X., Shen, L., Sun, B., and Jiang, L. (2010). An orthogonal curvature fibre bragg grating sensor array for shape reconstruction. *Commun. Comput. Inform. Sci.* 97, 25–31.

[38] Breedveld, P., Scheltes, J., Blom, E., and Verheij, J. (2005). A new, easily miniaturized steerable endoscope. *IEEE Eng. Med. Biol. Mag*. 26, 40–47.